# Helium in near earth orbit

J. Alcaraz, B. Alpat, G. Ambrosi, H. Anderhub, L. Ao, A. Arefiev, P. Azzarello, E. Babucci, Luca Baldini, M. Basile, et al.

# Helium in Near Earth Orbit

The AMS Collaboration

## Abstract

The helium spectrum from 0.1 to 100 GeV/nucleon was measured by the Alpha Magnetic Spectrometer (AMS) during space shuttle flight STS–91 at altitudes near 380 km. Above the geomagnetic cutoff the spectrum is parameterized by a power law. Below the geomagnetic cutoff a second helium spectrum was observed. In the second helium spectra over the energy range 0.1 to 1.2 GeV/nucleon the flux was measured to be $(6.3 \pm 0.9) \times 10^{-3} (\mathrm{m^2\,sec\,sr})^{-1}$ and more than ninety percent of the helium was determined to be $^3$He (at the 90 % CL). Tracing helium from the second spectrum shows that about half of the $^3$He travel for an extended period of time in the geomagnetic field and that they originate from restricted geographic regions similar to protons and positrons.

Submitted to *Phys. Lett. B*

# Introduction

Helium nuclei are the second most abundant element in cosmic rays. Helium rigidity spectrum measurements carried out over the past several decades (see [1] and references therein) have yielded insight into the origin of cosmic rays [2]. Since no difference in the rigidity spectra of protons and helium has been detected the same sources and propagation histories were inferred for both species [3]. However, recent and more accurate measurements [4, 5] suggest protons and helium may have different spectral indices in the range 10 to 100 GV. The most accurate experiments to date were balloon based [4,6–9], however in balloon experiments the $\sim 5$ g/cm$^2$ of residual atmosphere was an important source of systematic errors. Above $\sim$ 1000 GV emulsion experiments [10, 11] have indicated a more pronounced difference. Geomagnetically trapped low energy light isotopes have been studied with satellites [12].

The Alpha Magnetic Spectrometer (AMS) [13] is a high energy physics experiment scheduled for installation on the International Space Station. In preparation for this mission, AMS flew a precursor mission in June 1998 on board the space shuttle Discovery during flight STS–91 at altitudes between 320 and 390 km. In this report the data collected during that flight are used to study the cosmic ray helium spectra in the kinetic energy range 0.1 to 100 GeV/nucleon.

The high statistics ($\sim 10^6$) available allow measurement of the helium spectrum over a range of geomagnetic latitudes. With the incident particle direction and momentum accurately measured in AMS, the origin of particles below geomagnetic cutoff is studied by tracking them in the Earth's magnetic field.

# The AMS experiment

The major elements of AMS as flown on STS–91 were a permanent magnet, a tracker, time of flight hodoscopes, a Cerenkov counter and anti-coincidence counters [14, 15]. The permanent magnet had the shape of a cylindrical shell with inner diameter 1.1 m and length 0.8 m. It provided a central dipole field of 0.14 Tesla across the magnet bore and an analyzing power, $BL^2$, of 0.14 Tm$^2$ parallel to the magnet, or z–, axis. The six layers of double sided silicon tracker were arrayed transverse to the magnet axis. The outer layers were just outside the magnet bore. The tracker measured the trajectory of relativistic unit charge particles with an accuracy of 10 microns in the bending coordinate and 30 microns in the non-bending coordinate, as well as providing multiple energy loss measurements. The time of flight system had two orthogonal planes at each end of the magnet, covering the outer tracker layers. Together the four planes measured doubly charged particle transit times with an accuracy of 105 psec and they also yielded multiple energy loss measurements. A layer of anti-coincidence scintillation counters lined the inner surface of the magnet. Low energy particles were absorbed by thin carbon fiber shields. In flight the AMS positive z–axis pointed out of the shuttle payload bay.

Data collection started on 3 June 1998. The orbital inclination was 51.7° and the geodetic altitude ranged from 320 to 390 km. For this study the data was collected in three periods:

(a) 25 hours before docking with the MIR space station, during which the shuttle attitude was constrained to keep the AMS z–axis pointing within 45° of the zenith.

(b) Four days while docked to MIR. The AMS z–axis pointing varied between 40° and 145° of the zenith.

(c) After MIR undocking. Within 1 degree, the pointing was kept within 0°, 20° and 45° of the

zenith for 19, 25 and 20 hours. Before descending, the shuttle was turned over for approximately 9 hours and the pointing was towards the nadir.

Data collected while passing through the South Atlantic Anomaly were excluded from the analysis and the acceptance was restricted to events with an incident angle within 32° of the positive z–axis of AMS.

The response of the detector was simulated using the AMS detector simulation program, which is based on the GEANT package [16]. The effects of energy loss, multiple scattering, interactions [17], decays and the measured detector efficiency and resolution were included.

Postflight, the AMS detector was extensively calibrated [15] with helium and carbon beams at GSI, Darmstadt and with proton beams at the CERN PS. The helium calibration analyzed 30 million events at four different kinetic energy points from $E_K$ = 1.0 to 6.5 GeV/nucleon and at over six hundred incident angles and positions.

# Analysis

The incident particle rigidity, R = $pc/|Z|e$, was fit using two independent algorithms from the deflection of the trajectory measured using hits in at least 4 planes of the tracker. The velocity of the particle, $\beta$ = v/$c$, was determined using the information of the time of flight hits matching the reconstructed track. The mass of the particle was then determined from the measured velocity and momentum. To obtain $|Z|$, a reference set of energy loss distributions was obtained from the data samples and the energy measurements of the hits associated to the reconstructed particle were then fit to these reference distributions independently for the tracker layers and for the time of flight planes. For particles with $|Z| > 1$ the reconstruction was repeated requiring a higher threshold on the tracker hits. The particle type was then determined by combining the velocity, momentum and $Z$ measurements.

A particle was selected as a helium candidate if the determination of the charge magnitude from the measurements of energy losses in the tracker planes was $|Z| = 2$ and the particle type was compatible with a $|Z| > 1$ particle.

The main potential source of background to the helium sample were protons wrongly reconstructed as $|Z| = 2$ particles. Using the independent measurement of the charge magnitude obtained from the time of flight counters, as detailed in our earlier publication [15], this background was estimated to be less than $10^{-4}$ over all energies.

# Differential helium flux

The differential helium flux was determined by correcting the measured rates for the detector acceptance as a function of the particle momentum and direction. The acceptance was determined via the Monte Carlo method using simulated helium samples which were required to pass through a trigger simulation and the same reconstruction and selection chain as for data. The average acceptance was determined to be 0.10 $m^2$ sr for rigidities above 20 GV, increasing at lower rigidities to 0.16 $m^2$ sr.

Corrections to the acceptance were studied with a sample of events collected with an unbiased trigger and by comparing data and Monte Carlo samples. The average contributions to the uncertainty in these corrections were 4 % from the trigger, 3 % from the track reconstruction, and 2 % each from the modeling of particle interactions and from the selection; leading to an overall systematic error of 6% in the acceptance. The incident differential helium flux was obtained from an unfolding of the measured spectrum based on Bayes' theorem [18].

For the differential flux analysis, only the data sample from period (c) was considered. The differential spectra for three ranges of the corrected geomagnetic latitude [19], $|\Theta_M|$, are presented in Fig. 1 for the $0^\circ$ attitude subsample.

The figure shows the effect of the geomagnetic cutoff which decreases with increasing $|\Theta_M|$. In addition to the above cutoff, or primary, spectrum, Fig. 1 also shows the presence of a second spectrum below cutoff for $|\Theta_M| < 0.8$, which is discussed in detail below.

This cutoff effect varies weakly for the different attitudes ($0^\circ$, $20^\circ$, $45^\circ$) due to the anisotropy of the flux at these rigidity ranges. Above cutoff the flux spectra are identical. The differential primary helium spectrum versus rigidity using the combined above cutoff data from the three attitudes is presented in table 1 and in Fig. 2 scaled by $R^{2.74}$. For comparision, Fig. 2 also shows the helium flux used in atmospheric neutrino calculations [20].

| R | Flux |
|---|---|
| .76 – .91 | (32 ± 16) |
| .91 – 1.10 | 48.9 ± 2.9 |
| 1.10 – 1.32 | 58.4 ± 3.2 |
| 1.32 – 1.58 | 62.8 ± 3.4 |
| 1.58 – 1.91 | 63.9 ± 3.5 |
| 1.91 – 2.29 | 58.2 ± 3.2 |
| 2.29 – 2.75 | 49.4 ± 2.7 |
| 2.75 – 3.31 | 39.6 ± 2.1 |
| 3.31 – 3.98 | 30.8 ± 1.7 |
| 3.98 – 4.79 | 22.6 ± 1.2 |

| R | Flux |
|---|---|
| 4.79 – 5.75 | $(159. \pm 8.6) \times 10^{-1}$ |
| 5.75 – 6.92 | $(110. \pm 5.9) \times 10^{-1}$ |
| 6.92 – 8.32 | $(72.8 \pm 3.9) \times 10^{-1}$ |
| 8.32 – 10.00 | $(47.1 \pm 2.5) \times 10^{-1}$ |
| 10.00 – 12.02 | $(29.9 \pm 1.6) \times 10^{-1}$ |
| 12.02 – 14.45 | $(18.9 \pm 1.0) \times 10^{-1}$ |
| 14.45 – 17.38 | $(119. \pm 6.4) \times 10^{-2}$ |
| 17.38 – 20.89 | $(73.7 \pm 4.0) \times 10^{-2}$ |
| 20.89 – 25.12 | $(47.0 \pm 2.6) \times 10^{-2}$ |
| 25.12 – 30.20 | $(28.9 \pm 1.6) \times 10^{-2}$ |

| R | Flux |
|---|---|
| 30.20 – 36.31 | $(172. \pm 9.4) \times 10^{-3}$ |
| 36.31 – 43.65 | $(101. \pm 5.6) \times 10^{-3}$ |
| 43.65 – 52.48 | $(63.2 \pm 3.5) \times 10^{-3}$ |
| 52.48 – 63.10 | $(38.0 \pm 2.1) \times 10^{-3}$ |
| 63.10 – 75.86 | $(22.2 \pm 1.2) \times 10^{-3}$ |
| 75.86 – 91.20 | $(137. \pm 8.0) \times 10^{-4}$ |
| 91.20 – 109.65 | $(82.9 \pm 5.0) \times 10^{-4}$ |
| 109.65 – 131.83 | $(49.1 \pm 3.3) \times 10^{-4}$ |
| 131.83 – 158.49 | $(27.8 \pm 1.9) \times 10^{-4}$ |
| 158.49 – 190.55 | $(16.5 \pm 1.4) \times 10^{-4}$ |
| 190.55 – 229.09 | $(118. \pm 8.0) \times 10^{-5}$ |

Table 1: Differential primary helium flux in units of $(m^2\,\mathrm{sec}\,\mathrm{sr}\,\mathrm{GV})^{-1}$ versus rigidity, R, in GV. The errors quoted are the combination in quadrature of the statistical and systematic errors.

## Analysis of the primary spectrum

The primary cosmic ray spectrum may be parametrized by a power law in rigidity as $\Phi_0 \times R^{-\gamma}$. The spectrum has been fit [21] over the rigidity range $20 < R < 200$ GV. To avoid cutoff effects, data collected in regions where the expected cutoff in the direction of the AMS z–axis was larger than 12 GV were excluded from the fit. The results obtained on the three different attitude samples were the same within the errors. The combined fit yields:

$$\gamma = 2.740 \pm 0.010\,(\mathrm{stat}) \pm 0.016\,(\mathrm{sys}),$$

$$\Phi_0 = 2.52 \pm 0.09\,(\mathrm{stat}) \pm 0.13\,(\mathrm{sys}) \pm 0.14\,(\gamma)\ \frac{\mathrm{GV}^{2.74}}{\mathrm{m}^2\,\mathrm{sec}\,\mathrm{sr}\,\mathrm{MV}}\,.$$

The systematic uncertainty in $\gamma$ was estimated from the uncertainty in the track resolution (0.014) and the variation of the selection criteria (0.009). The third uncertainty quoted for $\Phi_0$ reflects the systematic uncertainty in $\gamma$. This fit is shown with the data in Fig. 2. In Fig. 3 the primary spectrum is compared to the recent balloon measurements [5, 7–9] [1)].

[1)] A $^3$He fraction of 0.15±0.05 was assumed.

## Analysis of the second spectrum

As shown in Fig. 1 a second spectrum is observed for $|\Theta_M| < 0.8$. This spectrum extends from the lowest measured rigidity, 0.8 GV, up to 3 GV with an integrated flux of $\sim 10^{-3}(\mathrm{m^2\,sec\,sr})^{-1}$.

To ensure these events are not due to resolution effects at low energies or to contamination from single scattering inside the detector, more stringent reconstruction criteria were applied in the examination of the second spectrum. Those $|Z| = 1$ events with a wrongly reconstructed charge magnitude were reduced by an additional factor of 100 by requiring the combined time of flight and tracker charge magnitude determinations to be $|Z| = 2$. Tails in the velocity reconstruction were reduced by requiring at least three matched hits in the four time of flight planes. In this energy range, the accuracy of the velocity measurement is 2.4%. Any large angle scattering in a tracker plane was identified and removed by requiring that the particle was also measured by the tracker in the non-bending projection and by requiring agreement between the rigidity measured with the first three hits along the track, with the last three hits and with all the hits. Events with collinear delta rays, which create additional energy depositions in the tracker planes along the trajectory of the particle, were identified and rejected by an isolation criteria on the amount of energy observed within 10 mm of the track. Finally, extrapolation of the fit track was required to match the location of the used time of flight counter hits within 60 mm.

These criteria were applied to the data samples from periods (a), (b) and (c). Compared to the looser cuts used in the analysis of the differential rigidity spectrum, the selection efficiency is ~ 65 % up to 3 GV. The average mass resolution for helium nuclei in the kinetic energy range 0.1 to 1.2 GeV/nucleon (*i.e.* $\beta < 0.9$) is ~ 12 %. Fig. 4 shows the reconstructed mass distribution for events above cutoff at $|\Theta_M| > 0.9$ in this energy range. As shown, the data are in agreement with a Monte Carlo simulation which contains 11.5 % $^3$He.

Fig. 5 shows the correlation between rigidity, R, and velocity, $\beta$, for events with $|\Theta_M| < 0.6$, together with the expectations for $^3$He and $^4$He nuclei. Primary spectrum events are clustered at $\beta > 0.9$ with rigidities in the range of 3 to 200 GV. A population of 115 events with rigidities below the local geomagnetic cutoff are marked in the figure with open circles. As seen, this population follows the $^3$He mass line. Fig. 6 shows a scatter plot of rigidity versus $\Theta_M$ for events with $\beta < 0.9$. The two symmetric clusters at $|\Theta_M| > 0.6$ correspond to nuclei from the primary helium spectrum. The same 115 events marked in Fig. 5 form a clear and isolated low energy band (R < 3 GV). This second population has the following properties:

- The reconstructed mass distribution given in Fig. 7 shows that most of the events are consistent with $^3$He. At the 90 % confidence level, the fraction of $^3$He exceeds ninety percent.
- As shown in Fig. 8, their spectrum extends from the lowest measured kinetic energy, $E_K$ = 0.1 GeV/nucleon, to ~ 1.2 GeV/nucleon, yielding an average flux of $(6.3 \pm 0.9) \times 10^{-3}(\mathrm{m^2\,sec\,sr})^{-1}$.
- As shown in Fig. 9, the flux tends to a maximum at the geomagnetic equator.
- Within the statistics, there is no preferred direction and the fluxes measured separately with data from the three periods (a), (b) and (c) are equal.

To understand the origin of these events, the trajectories have been traced both backward and forward from their incident angle, location and momentum, through the Earth's magnetic field, following the same procedure as described in [21, 22]. All events were found to originate in the atmosphere. Analysis of the sum of their forward and backward flight times yields two distinct classes: "short–lived" and "long–lived" for flight times below and above 0.3 sec respectively.

As shown in Fig. 10 the origins of the “short-lived” helium nuclei are distributed uniformly around the globe whereas the “long-lived” particles originate from two geographically restricted regions. These regions match those from which the second proton flux and second positron flux originate [21, 22]. Within the statistics, $^3$He is equally predominate in events from both the “short–lived” and “long–lived” classes.

# Conclusions

The helium spectrum between 0.1 and 100 GeV/nucleon was measured in near Earth orbit. The primary helium rigidity spectrum has been fit to a power law with a spectral index $\gamma = 2.740 \pm 0.010\,(\text{stat}) \pm 0.016\,(\text{sys})$. Below the geomagnetic cutoff a second spectrum of helium was observed with a flux of $(6.3 \pm 0.9) \times 10^{-3} (\text{m}^2\,\text{sec}\,\text{sr})^{-1}$. Over ninety percent of this second flux is $^3$He (at the 90 % CL). This second flux has been traced to originate from the same locations as the corresponding second proton and positron fluxes, with the long lived component originating from two restricted geographic regions.

# Acknowledgements

The support of INFN, Italy, ETH–Zürich, the University of Geneva, the Chinese Academy of Sciences, Academia Sinica and National Central University, Taiwan, the RWTH–Aachen, Germany, the University of Turku, the University of Technology of Helsinki, Finland, the U.S. DOE and M.I.T., CIEMAT, Spain, LIP, Portugal and IN2P3, France, is gratefully acknowledged.

The success of the first AMS mission is due to many individuals and organisations outside of the collaboration. The support of NASA was vital in the inception, development and operation of the experiment. Support from the Max–Planck Institute for Extraterrestrial Physics, from the space agencies of Germany (DLR), Italy (ASI), France (CNES) and China and from CSIST, Taiwan also played important roles in the success of AMS.

# References

[1] B. Wiebel-Sooth, P. L. Biermann and H. Meyer, Astr. and Astrophys **330** (1998) 389.

[2] P. L. Biermann *et al.,* Phys. Rev. **D51** (1995) 3450.

[3] W. R. Webber and J. A. Lezniak, Astrophys. Space Sci. **30** (1974) 361.

[4] E. S. Seo *et al.,* ApJ **378** (1991) 763.

[5] J. Buckley *et al.,* ApJ **429** (1994) 736–747.

[6] P. Papini *et al.,* Proc. 23rd ICRC Calgary **1** (1993) 579.

[7] M. Boezio *et al.,* ApJ **518** (1999) 457.

[8] T. Sanuki *et al.,* astro-ph/0002481 (2000).

[9] W. Menn *et al.,* ApJ **533** (2000) 281.

[10] K. Asakimori *et al.,* Proc. 23rd ICRC Calgary **2** (1993) 25.

[11] K. Asakimori *et al.,* ApJ **502** (1998) 278.

[12] J. P. Wefel *et al.,* Proc. 24th ICRC **4** (1995) 1021; J. Chen *et al.,* Geophys. Res. Lett. **21** (1994) 1583; M. D. Looper *et al.,* Radiation Measurements **26** (1996) 967; R. S. Selesnick and R. A. Mewaldt, JGR **101** (1996) 19745–19757.

[13] S. Ahlen *et al.,* Nucl. Inst. Meth. **A350** (1994) 351.

[14] G. M. Viertel and M. Capell, Nucl. Inst. Meth. **A419** (1998) 295–299.

[15] AMS Collaboration, J. Alcaraz *et al.,* Phys. Lett. **B461** (1999) 387–396.

[16] R. Brun *et al.,* GEANT 3, CERN DD/EE/84-1 (Revised, 1987); P. A. Aamio *et al.,* FLUKA Users Guide, CERN TIS-RP-190 (1990).

[17] R. J. Glauber, in: Lectures in Theoretical Physics, eds. W. E. Brittin *et al.***1** (N.Y. 1959) 315; S. Forte, Nucl. Phys. **A467** (1987) 665; S. Yu. Shmakov *et al.,* Comp. Phys. Comm. **54** (1988) 125; A. S. Pak *et al.,* Sov. J. Nucl. Phys. **30(2)** (1979) 178; I. V. Andreev and A. V. Chernov, Sov. J. Nucl. Phys. **28(2)** (1978) 243; Z. Omboo *et al.,* (1990), JINR-E. 90-21; G. Faldt and I. Hulthage, Nucl. Phys. **A316** (1979) 251; L. S. Azhgirei *et al.,* Sov. J. Nucl. Phys. **30(6)** (1979) 818; J. P. Burg *et al.,* Nucl. Phys. **B187** (1981) 205; A. Bujak *et al.,* Phys. Rev. **D23** (1981) 1895; V. Franco, Phys. Rev. **C6** (1972) 748; G. D. Alkhazov *et al.,* Nucl. Phys. **A280** (1977) 365; W. Bell *et al.,* Phys. Lett. **B117** (1982) 131; J. Jaros *et al.,* Phys. Rev. **C18** (1978) 2273; V. G. Ableev *et al.,* Z. Phys. **A340** (1991) 340; V. G. Ableev *et al.,* Acta physica Polonica **B16** (1985) 913; L. Satta *et al.,* Phys. Lett. **B139** (1984) 263.

[18] G. D'Agostini, Nucl. Inst. Meth. **A362** (1995) 487.

[19] A. Brekke, Physics of the Upper Polar Atmosphere, pp. 127–145, (Wiley, 1997).

[20] Formula 2.1 at solar minimum from M. Honda *et al.,* Phys. Rev. **D52** (1995) 4985, we have recently been informed that their current analysis is in closer agreement with our data. We thank M. Honda for this communication.

[21] AMS Collaboration, J. Alcaraz *et al.,* Phys. Lett. **B472** (2000) 215–226.

[22] AMS Collaboration, J. Alcaraz *et al.,* Phys. Lett. **B484** (2000) 10–22.

# The AMS Collaboration

J.Alcaraz[y], B.Alpat[ac], G.Ambrosi[r], H.Anderhub[ag], L.Ao[g], A.Arefiev[ab], P.Azzarello[r], E.Babucci[ac], L.Baldini[j,l], M.Basile[j], D.Barancourt[s], F.Barao[w,v], G.Barbier[s], G.Barreira[w], R.Battiston[ac], R.Becker[l], U.Becker[l], L.Bellagamba[j], P.Béné[r], J.Berdugo[y], P.Berges[l], B.Bertucci[ac], A.Biland[ag], S.Bizzaglia[ac], S.Blasko[ac], G.Boella[z], M.Boschini[z], M.Bourquin[r], L.Brocco[j], G.Bruni[j], M.Buenerd[s], J.D.Burger[l], W.J.Burger[ac], X.D.Cai[l], C.Camps[b], P.Cannarsa[ag], M.Capell[l], D.Casadei[j], J.Casaus[y], G.Castellini[p,j], C.Cecchi[ac], Y.H.Chang[m], H.F.Chen[t], H.S.Chen[i], Z.G.Chen[g], N.A.Chernoplekov[aa], T.H.Chiueh[m], Y.L.Chuang[ad], F.Cindolo[j], V.Commichau[b], A.Contin[j], M.Cristinziani[r], J.P.da Cunha[n], T.S.Dai[l], J.D.Deus[y], N.Dinu[ac,1], L.Djambazov[ag], I.D'Antone[j], Z.R.Dong[h], P.Emonet[r], J.Engelberg[u], F.J.Eppling[l], T.Eronen[af], G.Esposito[ac], P.Extermann[r], J.Favier[c], E.Fiandrini[ac], P.H.Fisher[l], G.Fluegge[b], N.Fouque[c], Yu.Galaktionov[ab,l], M.Gervasi[z], P.Giusti[j], D.Grandi[z], O.Grimm[ag], W.Q.Gu[h], K.Hangarter[b], A.Hasan[ag], V.Hermel[c], H.Hofer[ag], M.A.Huang[ad], W.Hungerford[ag], M.Ionica[ac,1], R.Ionica[ac,1], M.Jongmanns[ag], K.Karlamaa[u], W.Karpinski[a], G.Kenney[ag], J.Kenny[ac], W.Kim[ae], A.Klimentov[l,ab], R.Kossakowski[c], V.Koutsenko[l,ab], M.Kraeber[ag], G.Laborie[s], T.Laitinen[af], G.Lamanna[ac], G.Laurenti[j], A.Lebedev[l], S.C.Lee[ad], G.Levi[j], P.Levtchenko[ac,2], C.L.Liu[x], H.T.Liu[i], I.Lopes[n], G.Lu[g], Y.S.Lu[i], K.Lübelsmeyer[a], D.Luckey[l], W.Lustermann[ag], C.Maña[y], A.Margotti[j], F.Mayet[s], R.R.McNeil[e], B.Meillon[s], M.Menichelli[ac], A.Mihul[k], A.Mourao[v], A.Mujunen[u], F.Palmonari[j], A.Papi[ac], I.H.Park[ae], M.Pauluzzi[ac], F.Pauss[ag], E.Perrin[r], A.Pesci[j], A.Pevsner[d], M.Pimenta[w,v], V.Plyaskin[ab], V.Pojidaev[ab], M.Pohl[r], V.Postolache[ac,1], N.Produit[r], P.G.Rancoita[z], D.Rapin[r], F.Raupach[a], D.Ren[ag], Z.Ren[ad], M.Ribordy[r], J.P.Richeux[r], E.Riihonen[af], J.Ritakari[u], U.Roeser[ag], C.Roissin[s], R.Sagdeev[o], G.Sartorelli[j], A.Schultz von Dratzig[a], G.Schwering[a], G.Scolieri[ac], E.S.Seo[o], V.Shoutko[l], E.Shoumilov[ab], R.Siedling[a], D.Son[ae], T.Song[h], M.Steuer[l], G.S.Sun[h], H.Suter[ag], X.W.Tang[i], Samuel C.C.Ting[l], S.M.Ting[l], M.Tornikoski[u], J.Torsti[af], J.Trümper[q], J.Ulbricht[ag], S.Urpo[u], I.Usoskin[z], E.Valtonen[af], J.Vandenhirtz[a], F.Velcea[ac,1], E.Velikhov[aa], B.Verlaat[ag,3], I.Vetlitsky[ab], F.Vezzu[s], J.P.Vialle[c], G.Viertel[ag], D.Vité[r], H.Von Gunten[ag], S.Waldmeier Wicki[ag], W.Wallraff[a], B.C.Wang[x], J.Z.Wang[g], Y.H.Wang[ad], K.Wiik[u], C.Williams[j], S.X.Wu[l,m], P.C.Xia[h], J.L.Yan[g], L.G.Yan[h], C.G.Yang[i], M.Yang[i], S.W.Ye[t,4], P.Yeh[ad], Z.Z.Xu[t], H.Y.Zhang[f], Z.P.Zhang[t], D.X.Zhao[h], G.Y.Zhu[i], W.Z.Zhu[g], H.L.Zhuang[i], A.Zichichi[j], B.Zimmermann[ag], P.Zuccon[ac]

---

[a] I. Physikalisches Institut, RWTH, D-52056 Aachen, Germany[5]

[b] III. Physikalisches Institut, RWTH, D-52056 Aachen, Germany[5]

[c] Laboratoire d'Annecy-le-Vieux de Physique des Particules, LAPP, F-74941 Annecy-le-Vieux CEDEX, France

[e] Louisiana State University, Baton Rouge, LA 70803, USA

[d] Johns Hopkins University, Baltimore, MD 21218, USA

[f] Center of Space Science and Application, Chinese Academy of Sciences, 100080 Beijing, China

[g] Chinese Academy of Launching Vehicle Technology, CALT, 100076 Beijing, China

[h] Institute of Electrical Engineering, IEE, Chinese Academy of Sciences, 100080 Beijing, China

[i] Institute of High Energy Physics, IHEP, Chinese Academy of Sciences, 100039 Beijing, China[6]

[j] University of Bologna and INFN-Sezione di Bologna, I-40126 Bologna, Italy[7]

[k] Institute of Microtechnology, Politechnica University of Bucharest and University of Bucharest, R-76900 Bucharest, Romania

[l] Massachusetts Institute of Technology, Cambridge, MA 02139, USA

[m] National Central University, Chung-Li, Taiwan 32054

[n] Laboratorio de Instrumentacao e Fisica Experimental de Particulas, LIP, P-3000 Coimbra, Portugal

[o] University of Maryland, College Park, MD 20742, USA

[p] CNR–IROE, I-50125 Florence, Italy

[q] Max–Planck Institut für extraterrestrische Physik, D-85740 Garching, Germany

[r] University of Geneva, CH-1211 Geneva 4, Switzerland
[s] Institut des Sciences Nucleaires, F-38026 Grenoble, France
[t] Chinese University of Science and Technology, USTC, Hefei, Anhui 230 029, China[6]
[u] Helsinki University of Technology, FIN-02540 Kylmala, Finland
[v] Instituto Superior Técnico, IST, P-1096 Lisboa, Portugal
[w] Laboratorio de Instrumentacao e Fisica Experimental de Particulas, LIP, P-1000 Lisboa, Portugal
[x] Chung–Shan Institute of Science and Technology, Lung-Tan, Tao Yuan 325, Taiwan
[y] Centro de Investigaciones Energéticas, Medioambientales y Tecnologícas, CIEMAT, E-28040 Madrid, Spain[8]
[z] INFN-Sezione di Milano, I-20133 Milan, Italy[7]
[aa] Kurchatov Institute, Moscow, 123182 Russia
[ab] Institute of Theoretical and Experimental Physics, ITEP, Moscow, 117259 Russia
[ac] INFN-Sezione di Perugia and Universitá Degli Studi di Perugia, I-06100 Perugia, Italy[7]
[ad] Academia Sinica, Taipei 11529, Taiwan
[ae] Kyungpook National University, 702-701 Taegu, Korea
[af] University of Turku, FIN-20014 Turku, Finland
[ag] Eidgenössische Technische Hochschule, ETH Zürich, CH-8093 Zürich, Switzerland
[1] Permanent address: HEPPG, Univ. of Bucharest, Romania.
[2] Permanent address: Nuclear Physics Institute, St. Petersburg, Russia.
[3] Now at National Institute for High Energy Physics, NIKHEF, NL-1009 DB Amsterdam, The Netherlands.
[4] Supported by ETH Zürich.
[5] Supported by the Deutsches Zentrum für Luft– und Raumfahrt, DLR.
[6] Supported by the National Natural Science Foundation of China.
[7] Also supported by the Italian Space Agency.
[8] Also supported by the Comisión Interministerial de Ciencia y Tecnología.

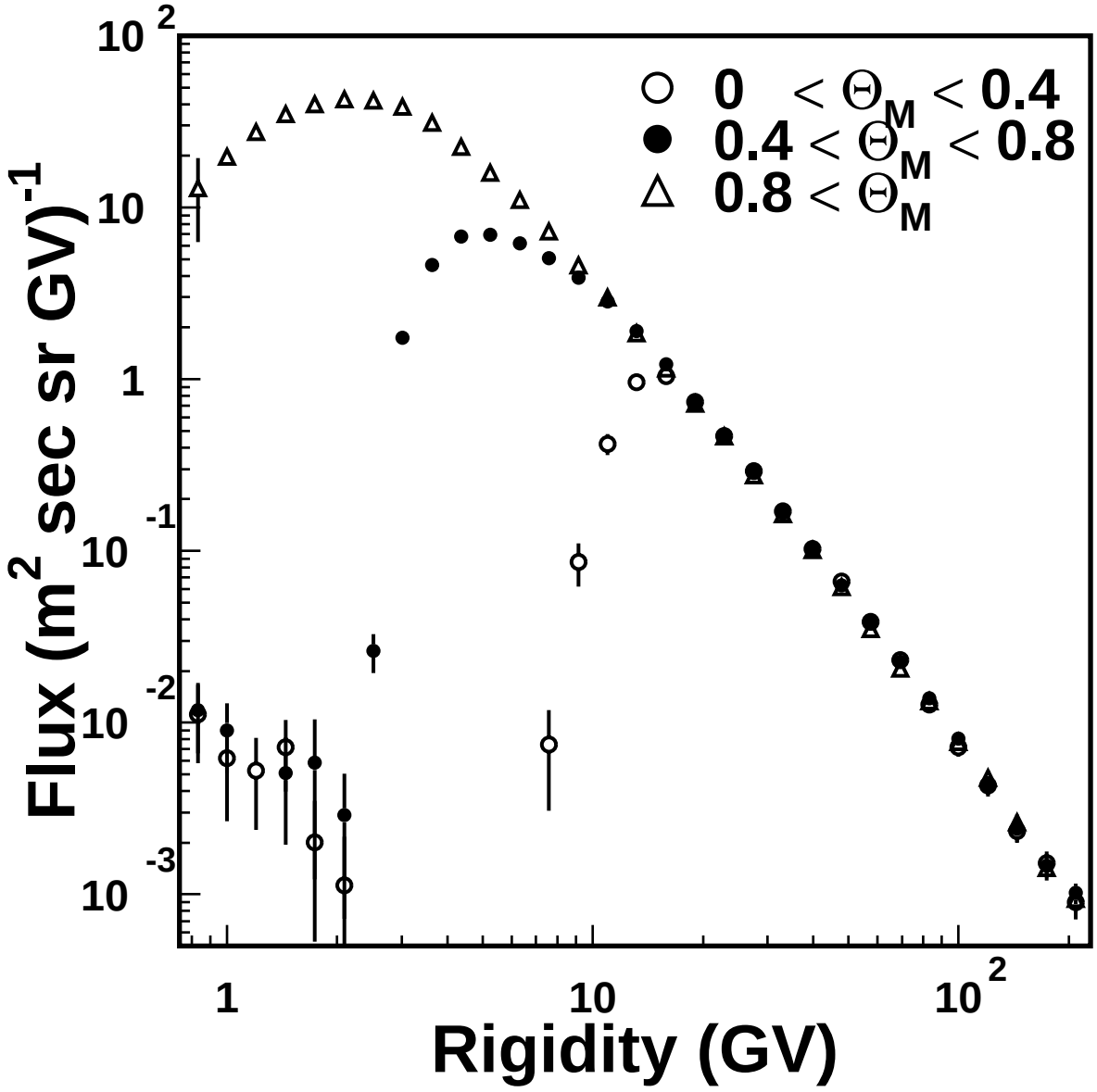


Figure 1: Helium flux spectra for the zenith pointing separated according to the geomagnetic latitude, $|\Theta_M|$, at which they were detected.

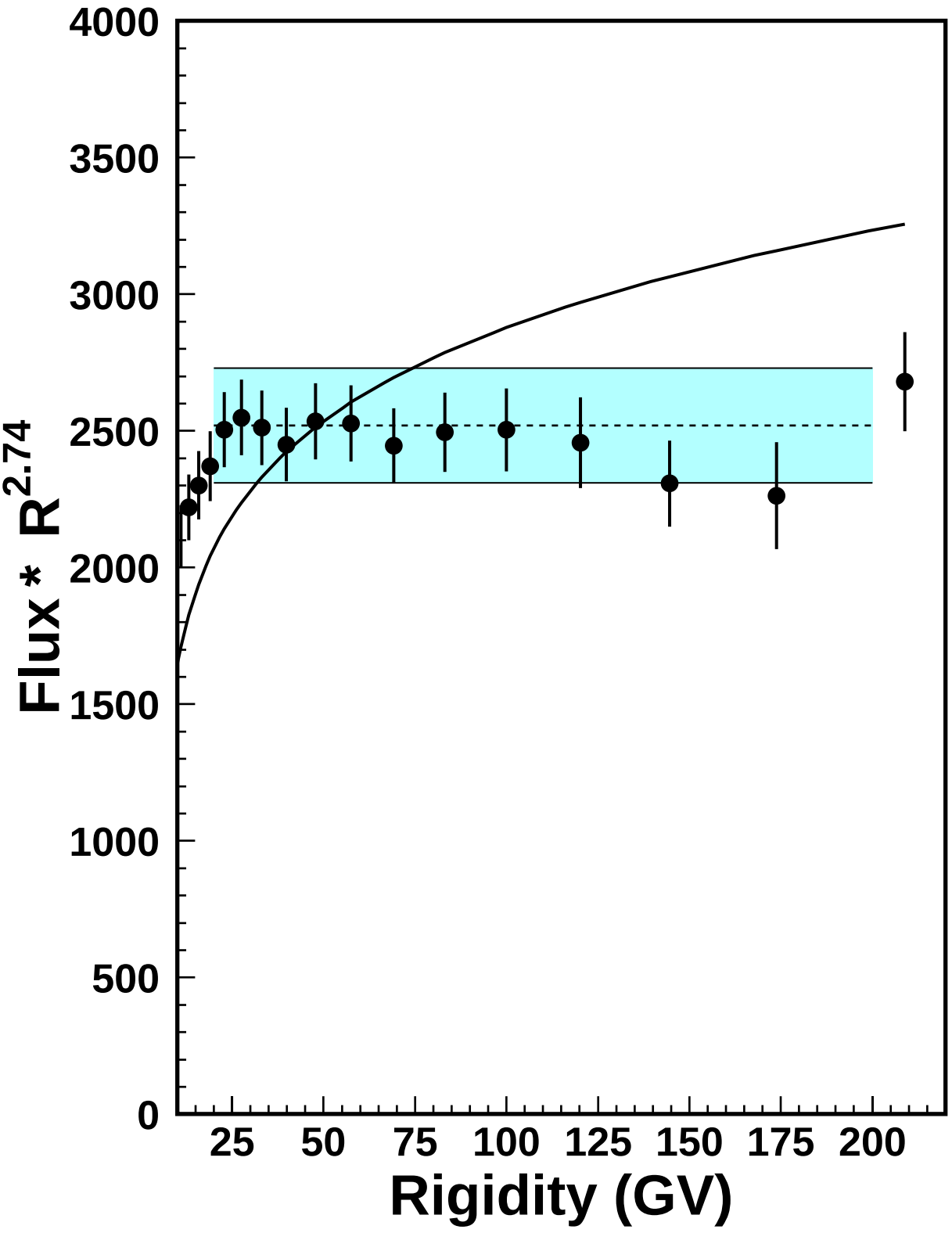


Figure 2: Primary helium flux spectrum multiplied by $R^{2.74}$ in units of $m^{-2}\,sec^{-1}\,sr^{-1}\,GV^{1.74}$. The band covers the range of the fit. The smooth line shows the spectrum used for atmospheric neutrino spectrum calculations [20].

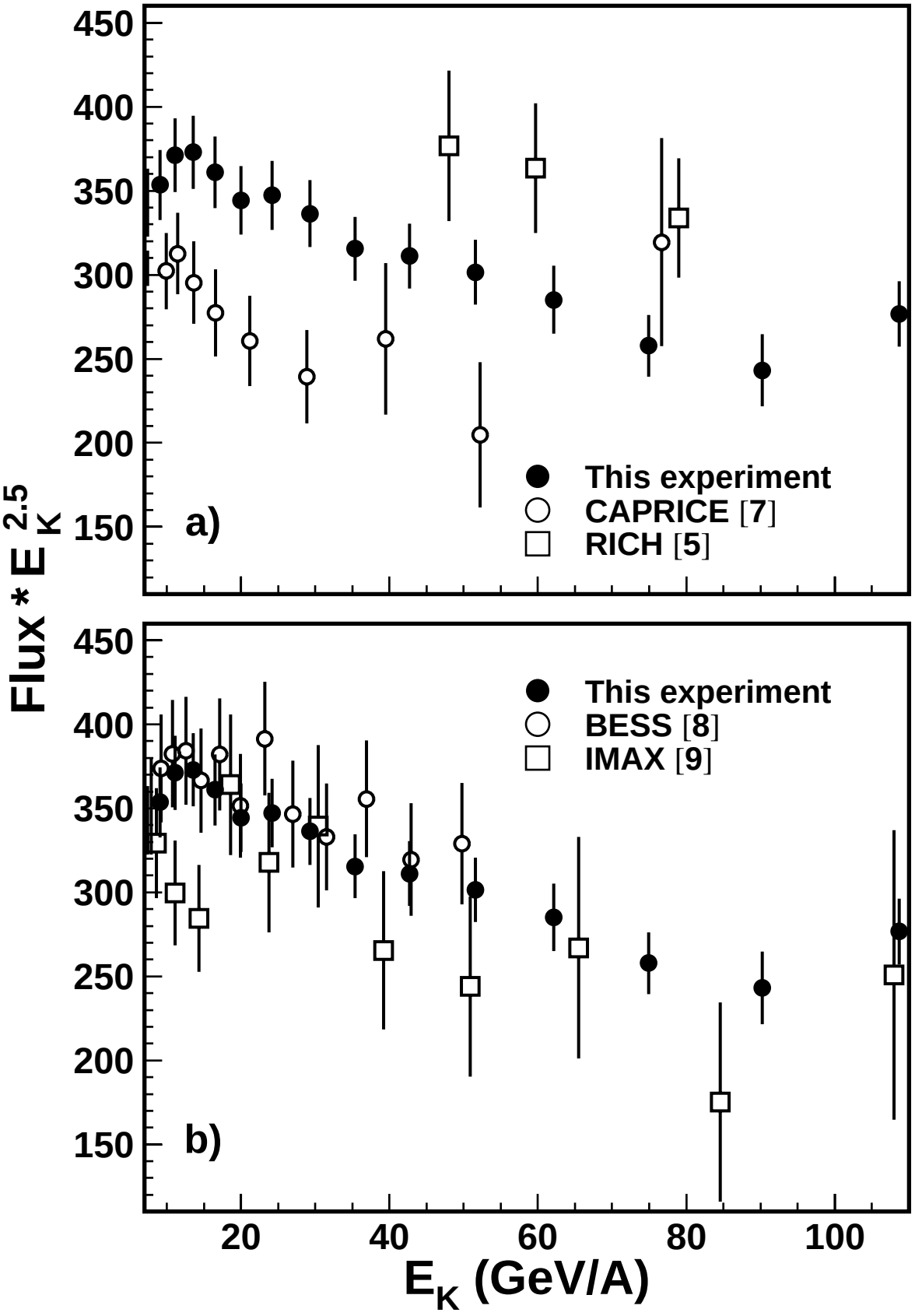


Figure 3: Comparison with recent measurements of the primary helium flux spectrum multiplied by $E_K^{2.5}$ in units of $m^{-2}\ sec^{-1}\ sr^{-1}\ (GeV/A)^{1.5}$.

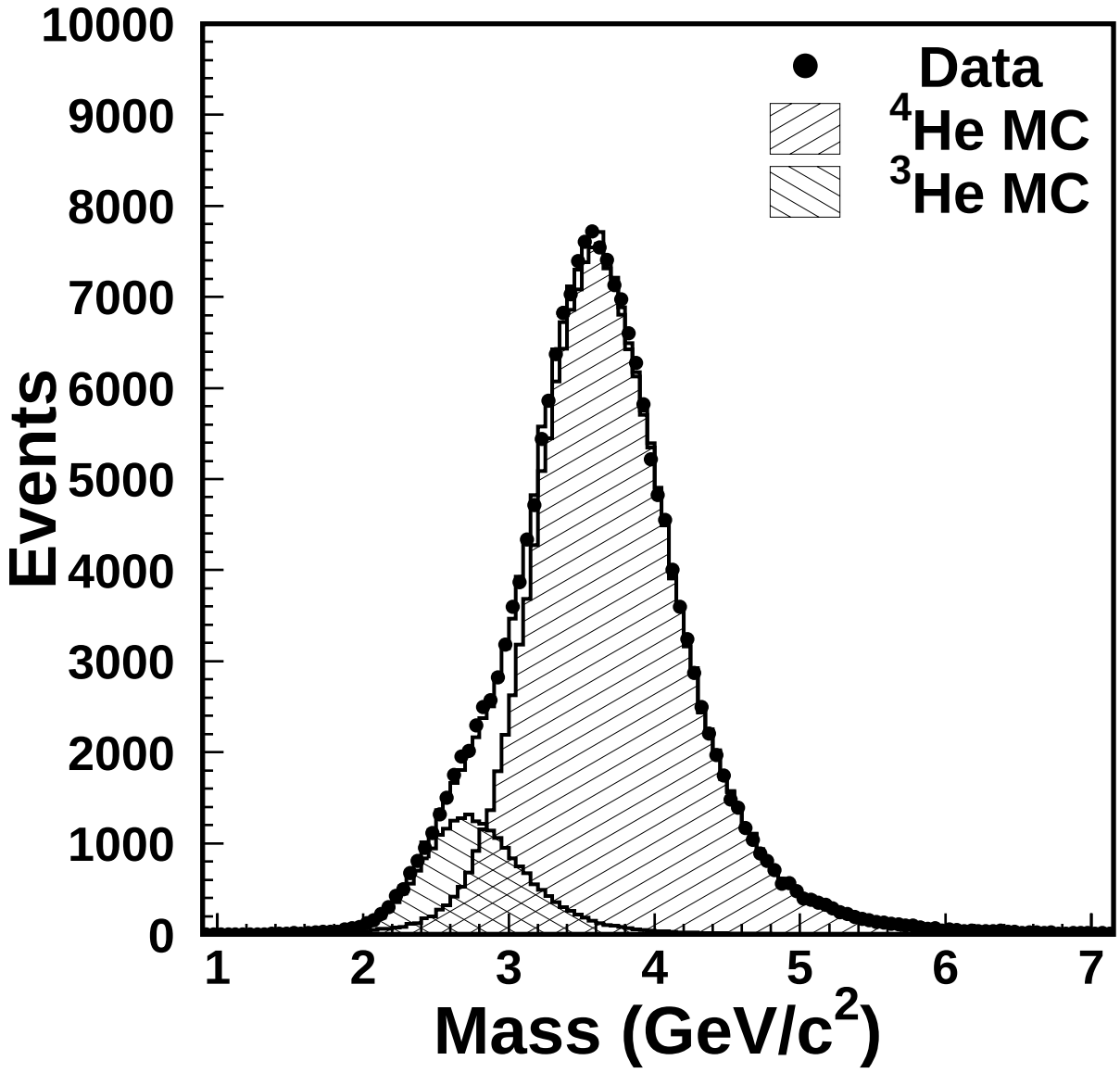


Figure 4: Mass distribution for helium events above geomagnetic cutoff for $|\Theta_M| > 0.9$ and $\beta < 0.9$. Filled circles are data for period (c). Histogram is a Monte Carlo simulation with 11.5 % $^3$He.

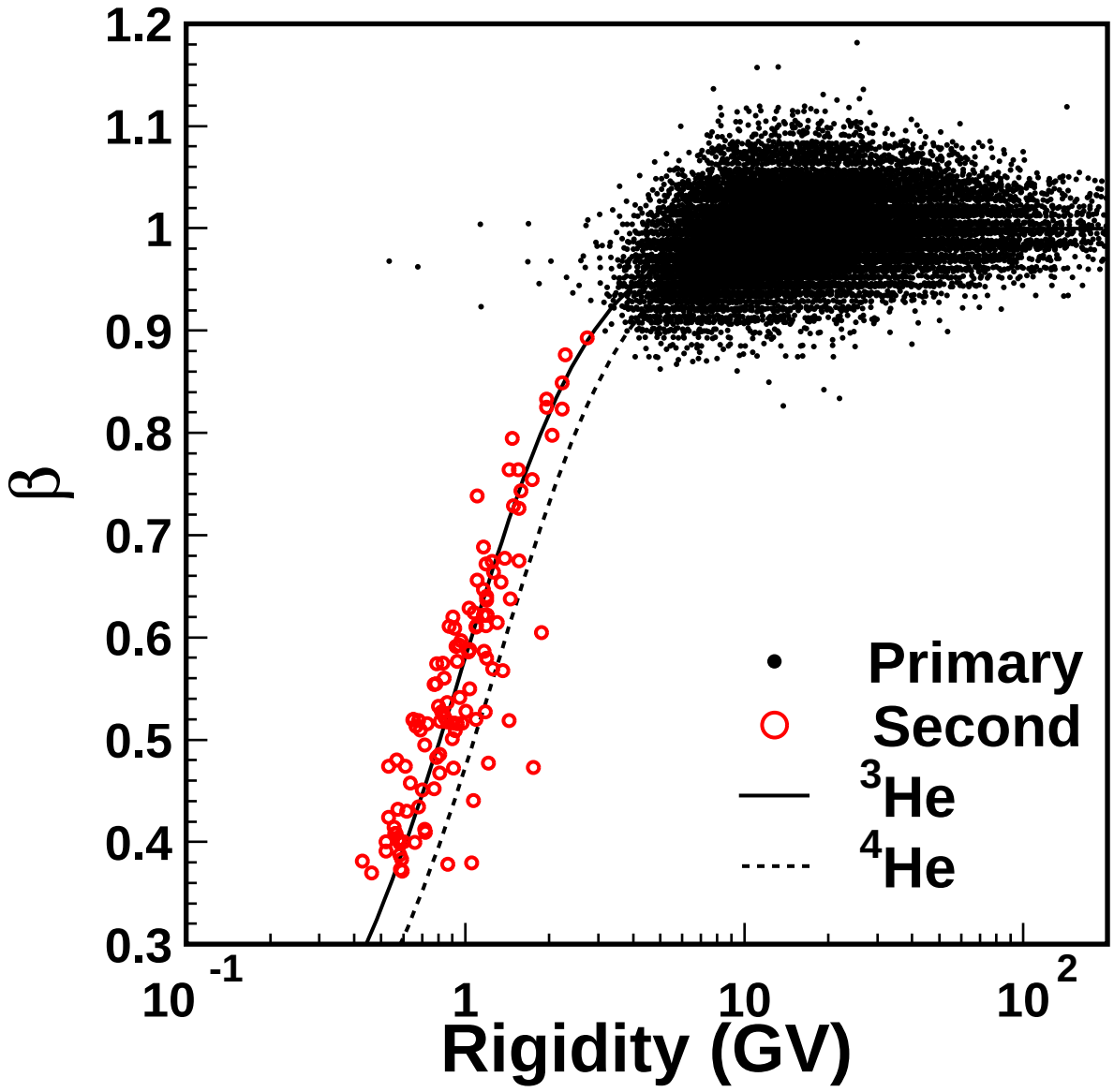


Figure 5: Correlation between rigidity and velocity for helium events detected at $|\Theta_M| < 0.6$. Dots denote events from the primary spectrum, and open circles those from under cutoff. The solid (dashed) line corresponds to $^3$He ($^4$He).

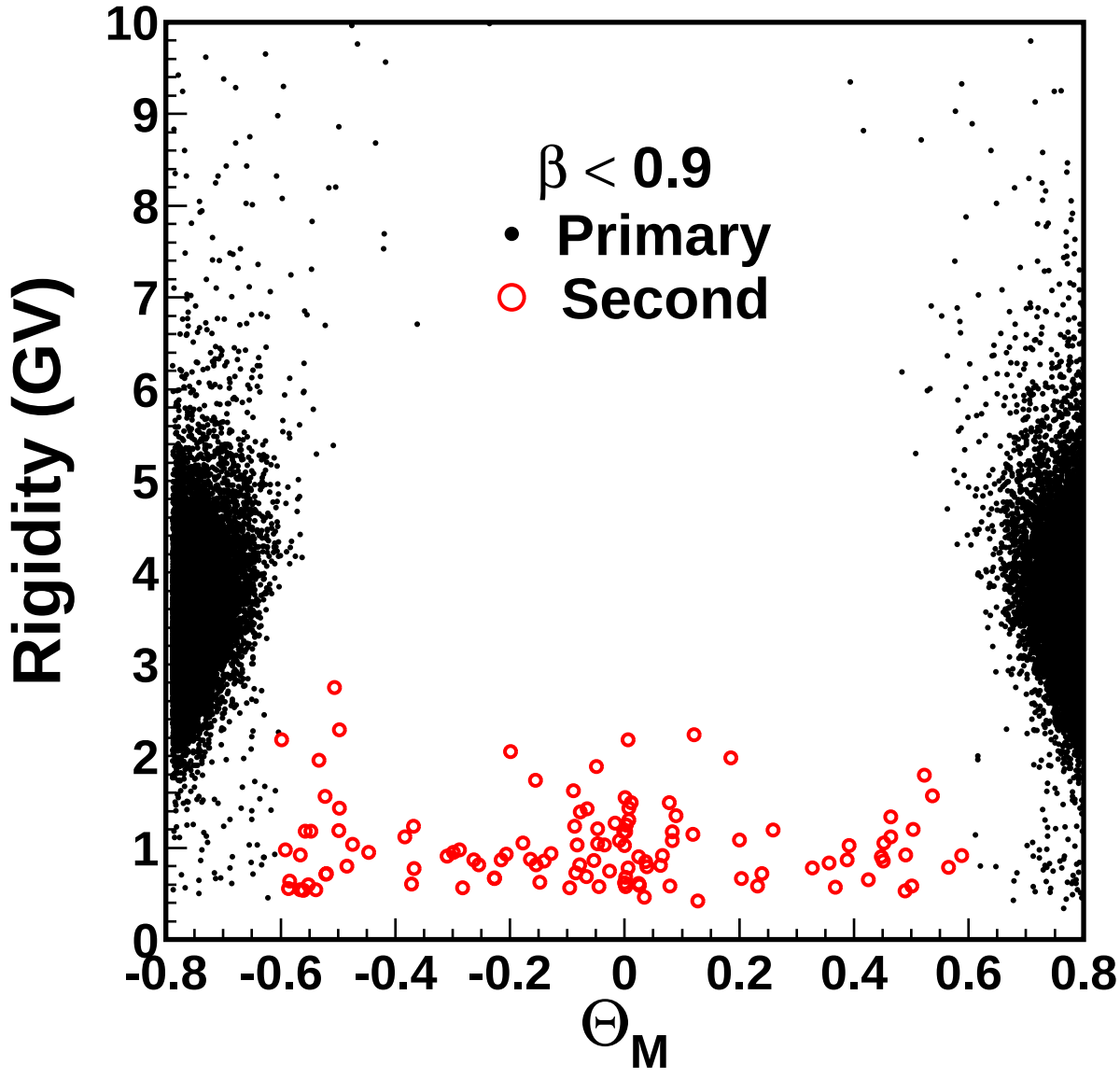


Figure 6: Rigidity versus $\Theta_M$ for events with $\beta < 0.9$. Dots and open circles as in Fig. 5.

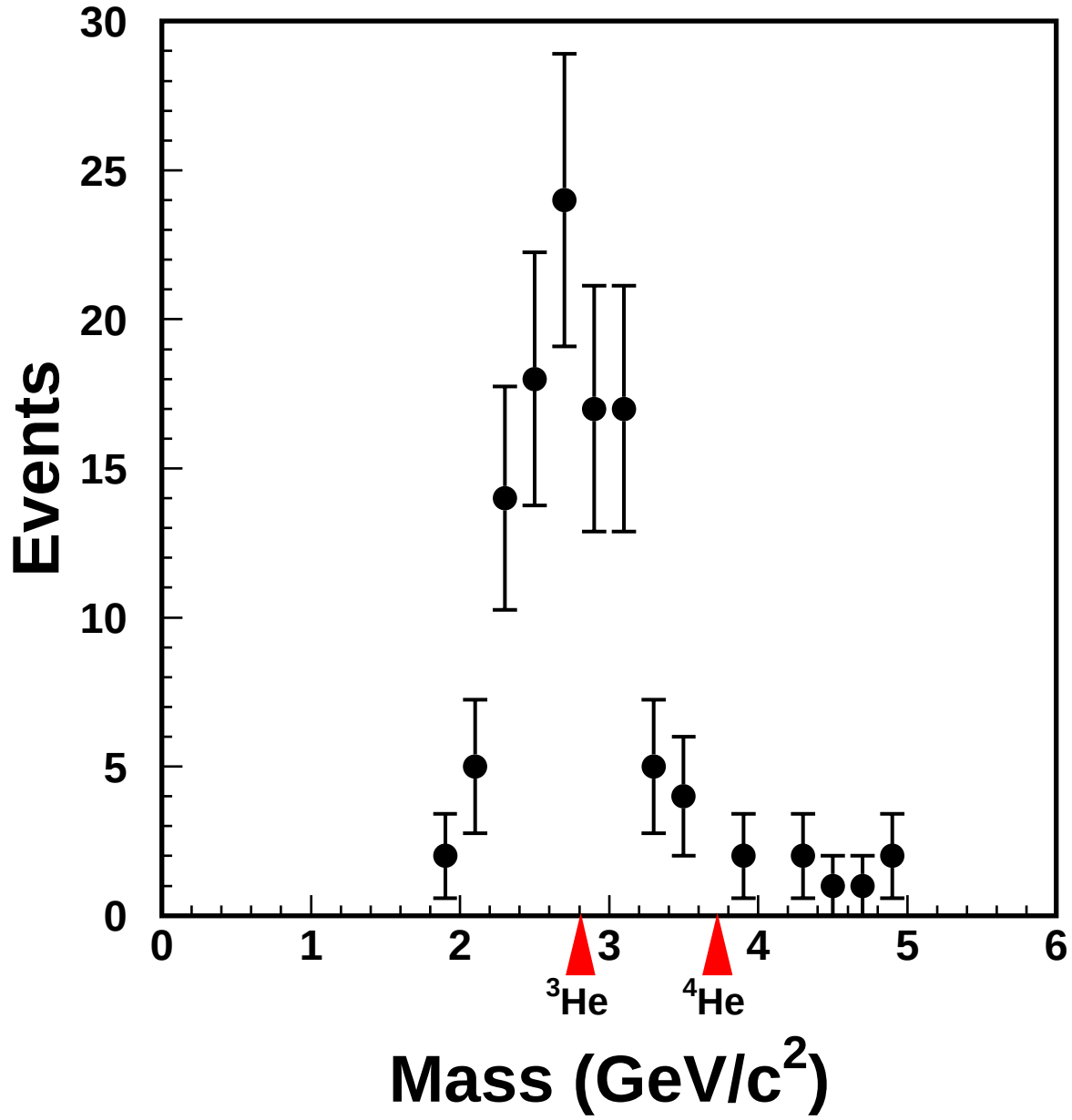


Figure 7: Reconstructed mass distribution for the second spectrum helium for $|\Theta_M| < 0.6$ compared with the masses of $^3$He and $^4$He.

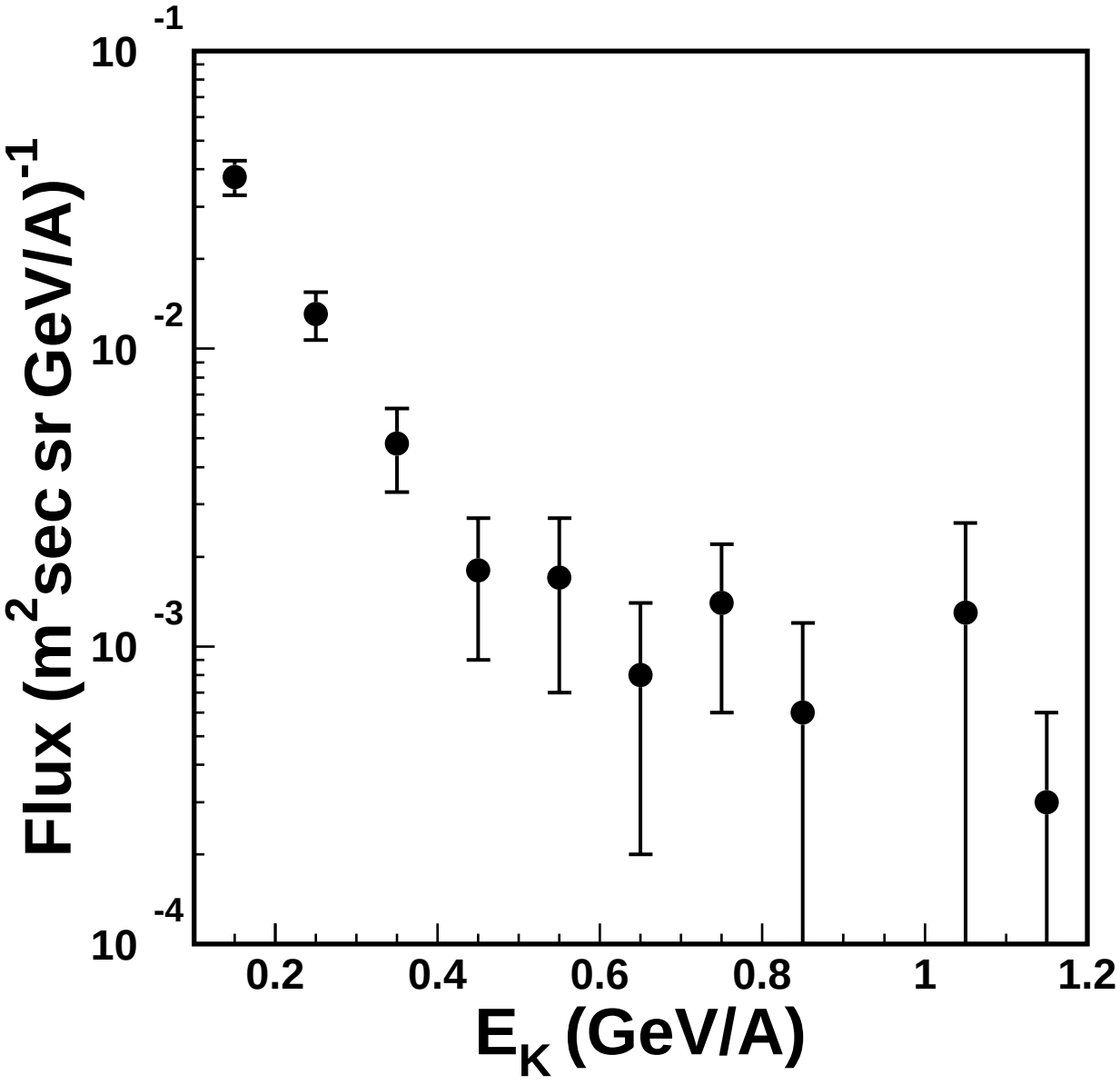


Figure 8: Second helium flux spectra for $|\Theta_M| < 0.6$.

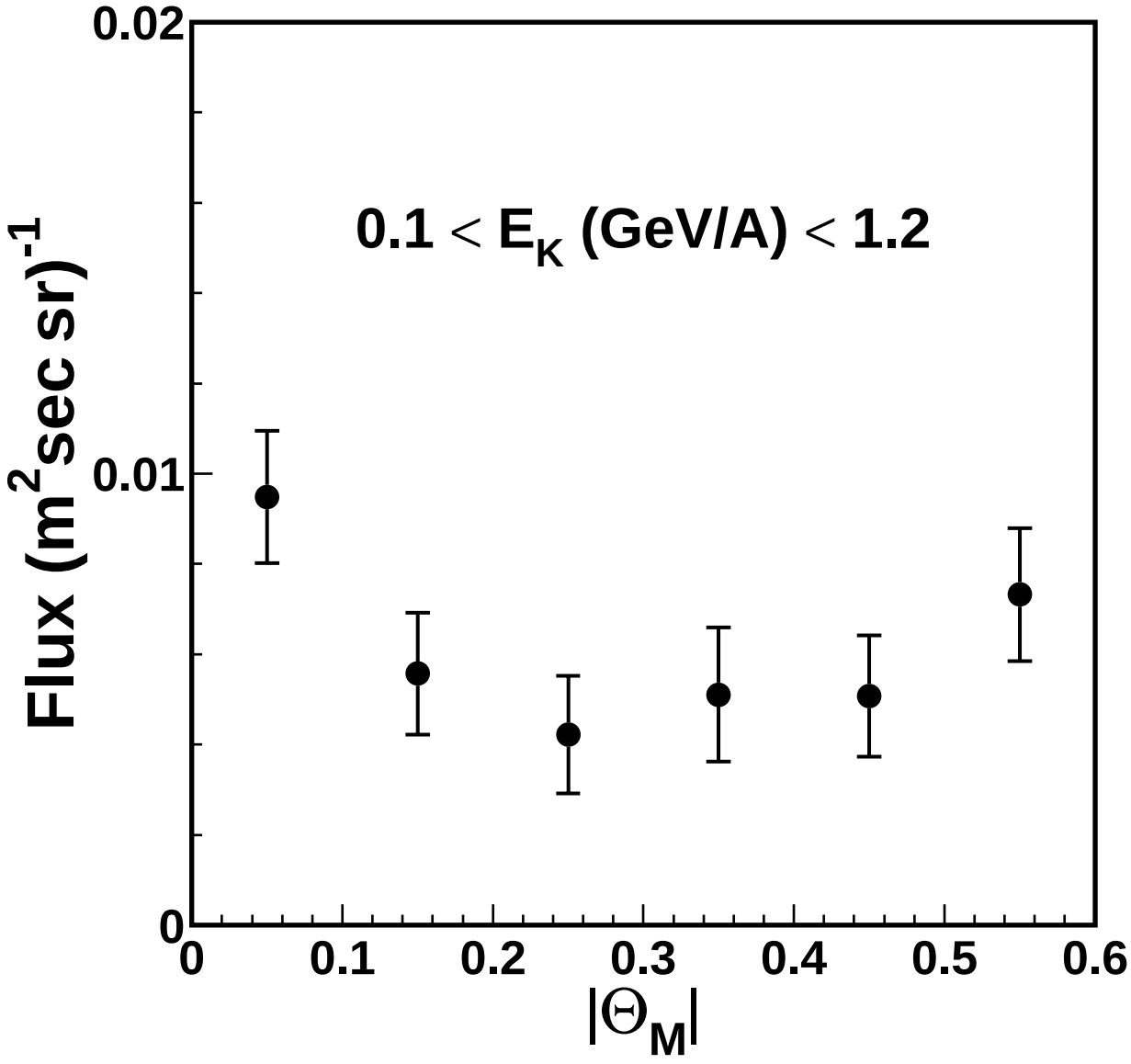


Figure 9: Average flux of the second helium spectrum versus geomagnetic latitude.

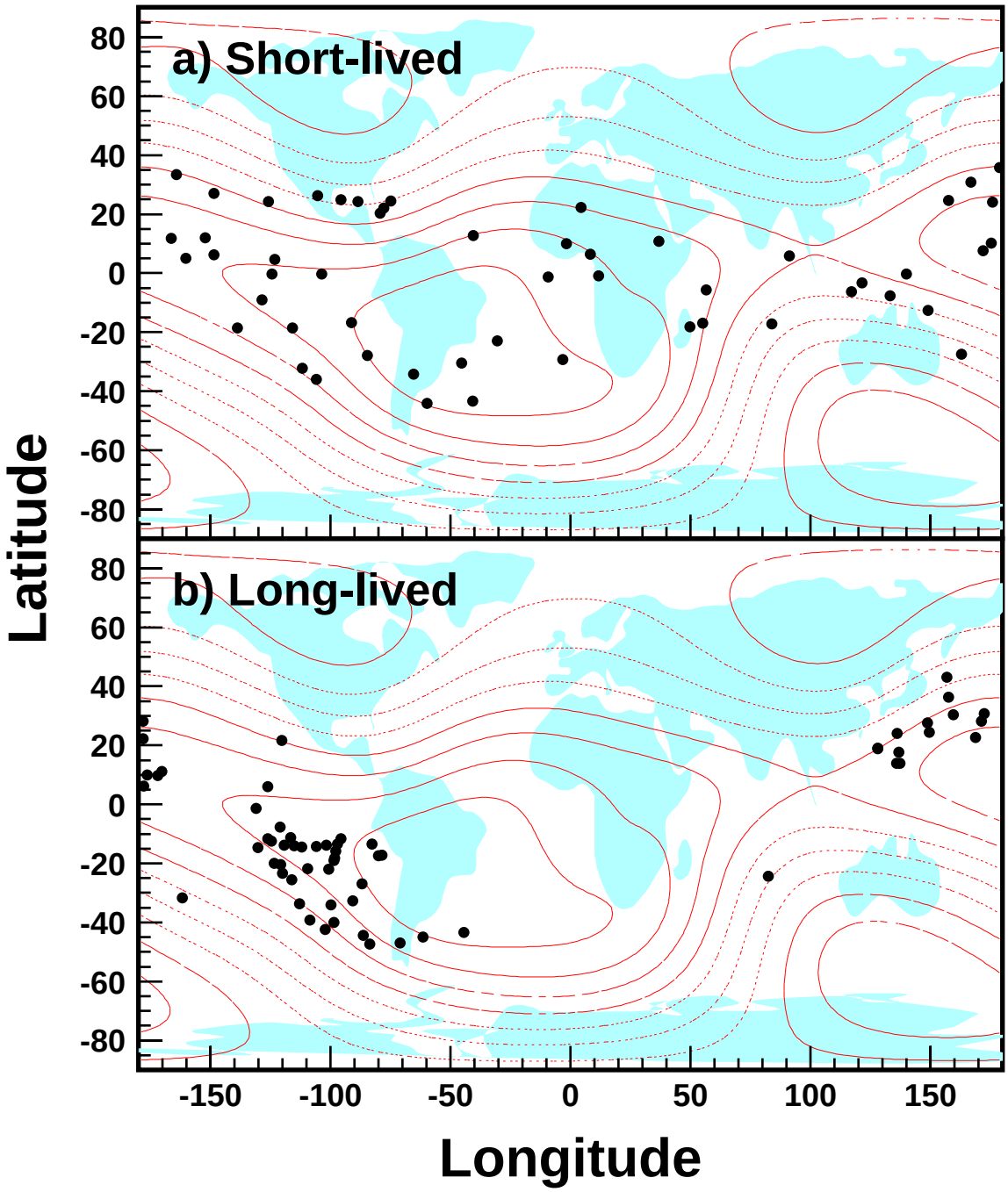


Figure 10: Geographical origin of a) “short-lived” and b) “long-lived” helium in the second spectrum. The lines indicate the geomagnetic field contours at 380 km.